1 Scanning Near-field Optical Studies of Photonic Devices

V. Sandoghdar[1(a)], *B. Buchler*[(a)], *P. Kramper*[(b)], *S. Götzinger*[(c)], *O. Benson*[(c)] *and M. Kafesaki*[(d)]

(a) Laboratorium für Physikalische Chemie, Eidgenossische Technische Hochschule (ETH), CH-8093 Zurich, Switzerland
(b) CNRS/LPN, route de Nozay, 91460 Marcoussis, France
(c) Humboldt-Universität zu Berlin, Institut für Physik, Hausvogteiplatz 5-7, 10117 Berlin, Germany
(d) Research Center of Crete, Heraklion, Crete, Greece

1.1 Introduction

Visualization and manipulation of optical processes at the sub-wavelength scale has important applications in a wide range of science and technology. High resolution optical lithography has, for instance, been the key to the rapid progress of the chip industry while modern techniques in fluorescence microscopy have opened new doors in biological and medical research. The photonics community has both benefited from, and contributed to, the advance of sub-wavelength optics. From the conceptual point of view, photonics researchers are interested in manipulating optical phenomena in confined geometries to realize more efficient and versatile miniaturized optical devices. From the application side, once a structure has been fabricated, it has to be characterized and tested using high resolution optical microscopy and spectroscopy.

Among various photonic devices, photonic crystals (PhCs) are perhaps the prime candidates for high resolution studies. By definition, light inside a PhC undergoes substantial changes both in phase and amplitude over distances much smaller than a wavelength. Imaging the flow of light through the crystal structure would be highly advantageous for characterization of devices and comparison with numerical models. Application of conventional optical microscopy to photonic crystal devices is of only limited use since the resolution is limited by diffraction to about half the wavelength of light. To overcome the diffraction limit, scanning near-field optical microscopy (SNOM) can be applied. As we will see, SNOM techniques let us study the behavior of light at sharp bends in a PhC waveguide, allow us to make absolute measurement of transmission losses and reflection coefficients at junctions, make it possible to visualize the subwavelength spatial extent of the mode in a point defect microcavity and let us identify tiny imperfections in the fabrication of PhCs.

[1]Corresponding author: e-mail: vahid.sandoghdar@ethz.ch

1.2 Scanning Near-field Optical Microscopy (SNOM)

1.2.1 Brief historical background

In the 1980s microscopy witnessed a big revolution when scanning probe microscopes (SPM) were invented. Scanning tunnelling microscope (STM) and the atomic force microscope (AFM) offered atomic resolution in surface studies, and although they are not suitable for optical experiments, their technological development has had important consequences for the realization of the third member of the SPM family, the scanning near-field optical microscope (SNOM).

After the pioneering works of two independent groups around D. Pohl [1] at IBM Zurich and A. Lewis [2] at Cornell University in the years 1983–1984, it took several more years of technical development before the advantages of SNOM could be exploited in different applications in the 1990s. The most valuable contribution towards a reliable device was the discovery of a convenient tip-sample distance stabilization in 1992 by Toledo-Crow *et al.* [3] and Betzig *et al.* [4]. Perhaps the most spectacular scientific goal achieved with the SNOM was the detection of single fluorescent molecules at room temperature in 1993 [5]. During two decades many different configurations of illumination and detection as well as several concepts of probe design have been examined [6]. In the next section we will give a brief review of these with a particular eye on the applications of SNOM for photonics. More detailed and thorough treatments of SNOM can be found in the literature [6–10].

1.2.2 The operation principle of SNOM

Let us consider the situation in figure 1.1. A sample is illuminated with light of wavelength λ (we are not interested in the details of the illumination process at this point) and part of the incident light is reflected or transmitted. We can consider the sample to be a Fourier sum of many periodic gratings. Those gratings with periods greater than $\lambda/2$ will give rise to a diffraction pattern. Gratings with periods less than $\lambda/2$ will, on the other hand, only give rise to zeroth order diffraction which carries no spatial information about the grating. As a result, one cannot learn about a sample's sharp corners and rapid changes of the optical contrast if one collects the light that *propagates* away from the sample. This was pointed out by Abbé [11] in the 1870s who formulated a rigorous limit of $\lambda/2n\sin\theta$ to the resolution of an optical microscope with a full collection angle of 2θ in a medium of refraction index n.

Although Abbé's limit is quite robust, it only holds for the propagating waves. The interaction of high spatial frequency gratings with light also results in a surface dwelling evanescent

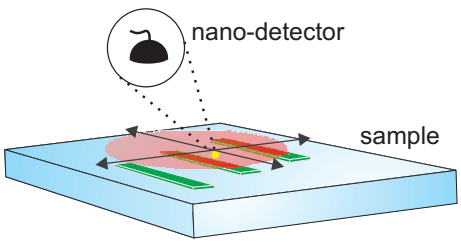

Figure 1.1: A nano-detector can be scanned to measure the intensity of the nonpropagating evanescent fields on the surface of a sample. The red region displays the illuminated area.

field [12], the strength of which is directly related to the optical contrast of the sample. The essence of near-field microscopy is to measure these non-propagating fields with subwavelength resolution by scanning a very small local detector close to the sample surface (see fig. 1.1). Two parameters decide on the performance of a SNOM in a fundamental manner. First, the size of the detector determines the resolution. A finer probe is usually desirable because it can scatter the evanescent field more locally and yield a higher resolution. One must, however, bear in mind that the strength of scattering processes typically scales as a power law so that better resolution is accompanied by a weaker signal. The second important factor is the distance between the probe and the sample. The evanescent field associated with a certain spatial frequency, κ, loses strength rapidly over distances of order $1/\kappa$. It is, therefore, important that the probe explores the sample surface as closely as possible. Scanning the sample at larger distances means not detecting the higher spatial frequency components and therefore lower resolution.

Aside from the probe size and its distance to the sample, several issues such as the polarization of light as well as illumination and detection configurations strongly influence SNOM images. A thorough and quantitative treatment of the imaging process in SNOM remains a challenge for both experimentalists and theorists alike. From the experimental point of view it is difficult to characterize each individual probe and sample to the extent that the measurement results could be interpreted in a fully quantitative manner. The theory on the other hand, is confronted by the challenge of performing three-dimensional numerical calculations, taking into account all geometric and material properties of realistic samples. In the following we provide a minimum working knowledge of near-field microscopy to set the ground for discussing its applications to photonics.

1.2.3 Instrumentation

Figure 1.2a shows the schematics of the main components of a SNOM setup. As in any SPM the heart of the setup is the tip. Depending on the mode of operation SNOM tips can be made of glass, metal or semiconductors, each either naked or coated. We focus our attention on glass fibre tips which can be made either by chemical etching or by heat pulling of optical fibres [6]. In most applications the tip is coated by a metallic layer from all sides except at the very end, leaving a subwavelength aperture. It is important that the coating is thick enough to prevent leakage through the metal. Leakage is also minimized by choosing a metal with small skin depth such as aluminium.

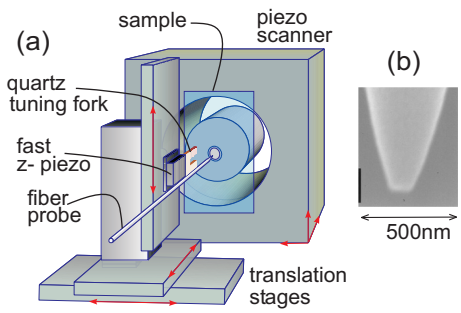

Figure 1.2: a) Schematic drawing of the SNOM machinery. A tip is mounted on a quartz tuning fork. The probe can be positioned against the sample using coarse translation stages and a piezoelectric scanner unit. b) Electron microscope image of glass fibre tip.

As argued above, the tip has to be positioned at a separation much smaller than a wavelength. This is a nontrivial task because a sharp tip is very fragile and any accidental contact with the surface could ruin it. To control the tip-sample distance a servo-loop based on the 'shear-force' interaction [3, 4] can be used. Shear force control relies on the not fully understood fact that the amplitude of a fibre tip oscillating parallel to a surface is damped when the tip approaches within 10-20 nm of the surface. There are various techniques for exciting and detecting the fibre oscillation [6], but the most common method is to glue the fibre to a prong of a tuning fork with an oscillation frequency about 32kHz (see figure 1.2a) [13]. The shear-force interaction of the fibre tip with the surface modifies the amplitude and phase of the fork oscillation which can be used to keep the distance separation between the tip and the sample constant. A bonus of this procedure is that one also obtains a topographic map of the sample surface via the piezo voltage, which is regulated to keep the shear-force signal constant. Piezoelectric elements are used to scan the sample relative to the probe or vice versa. In general, great care should be paid to the stability of the mechanical components against vibrations and drifts.

1.2.4 Various modes of SNOM operation

In photonics applications we are mostly interested in investigating the propagation of light in a device or its confinement to various regions. The majority of SNOM experiments reported in the literature, however, aim at optical microscopy in the conventional sense of characterizing sample features such as size, form, color and index of refraction. To put the configurations discussed in later sections in the broader context, we now briefly mention some of the other SNOM arrangements that are often encountered in the literature. Depending of how the sample is illuminated and the signal is detected, different modes of operation can be identified. These are not hard and fast categories, combinations can be, and are, used.

In the most common mode, a tapered optical fibre is aluminum coated at an angle so that a very small subwavelength opening is left at the front. This is an 'apertured' mode of SNOM. When light is coupled into the fibre it is mostly back reflected, but some reaches the small aperture where it induces electronic oscillations in the metallic layer. This oscillation results in the production of nonpropagating fields at the aperture exit as well as the emission of propagating radiation. When the tip is brought close to a sample the evanescent components are scattered into the far field and then detected either in transmission (figure 1.3a) or reflection. We refer to this configuration as the 'illumination mode'. In the reverse mode known as the 'collection mode' one illuminates the sample globally and detects through the apertured fibre tip (figure 1.3b).

In so-called 'apertureless SNOM' [14], one illuminates the sample globally and uses a solid metallic or dielectric tip to scatter the evanescent waves into the far field where they are detected (figure 1.3c). Some samples are suited to a third type of illumination via total internal reflection [15, 16] as shown in figure 1.3d. In this case light is introduced into a transparent sample in such a way that it undergoes total internal reflection. On the surface a SNOM tip is introduced to scatter the evanescent waves present due to the internally reflected light. The scattered light can be detected using apertured or non-apertured techniques. This arrangement is sometimes thought of as the optical equivalent of the STM in the sense that the photons that would have been otherwise evanescent can tunnel through the gap between the

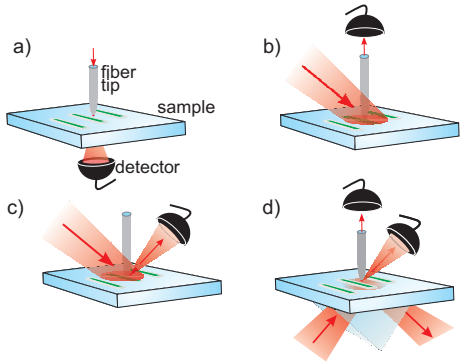

Figure 1.3: a) Illumination SNOM: the fibre is used to illuminate the sample. b) Collection SNOM: the sample is illuminated globally and evanescent fields are scattered by a sharp tip and collected through the fibre. c) Apertureless SNOM: the sample is illuminated globally. An "apertureless" tip is used to scatter the light into the far field. d) The sample is illuminated via total internal reflection. A tip is used to scatter the evanescent field into the fibre (collection mode) or the far-field (apertureless mode).

glass fibre and the sample. For this reason it has been also referred to as the photon scanning tunnelling microscopy (PSTM). It is, perhaps, more appropriate to talk about scattering instead of tunnelling when one of the bodies, in this case the tip, has subwavelength dimensions. For this reason we prefer to keep the terminology general and refer to all the different modes simply as SNOM.

1.3 Imaging Photonic Devices with SNOM

One of the early experiments that demonstrated how the high spatial resolution of SNOM could be useful for investigating photonic devices was reported by Choo *et al.* [17]. These authors mapped the intensity distribution in a channel waveguide and directional coupler by using SNOM. At about the same time a fibre tip was used to perform spatial mode mapping of the whispering-gallery modes (WGMs) in a high-finesse microresonator [18, 19]. Since the mid 1990s several groups have applied this technique to investigate light propagation and confinement in waveguides [20–23], laser diodes [24], VCSELs [25], microdisks [26], microrings [27], fibres [28] and photonic crystal structures [29–43].

Although our discussion will mostly focus on the work performed in our own laboratories, in the rest of the chapter we will endeavour to present an overview of SNOM and its application to photonic devices and photonic crystals. There are various SNOM techniques that have yet to be applied to photonic crystal structures. These will be discussed so as to highlight the potential that SNOM has for future experiments. We start, in the following section, with a simple introduction to SNOM experiments by presenting a measurement of the evanescent field formed by total internal reflection. In section 1.3.2 we discuss SNOM experiments on silica microspheres. As we will see, the complexity of this system makes it a very good example for elaborating on various issues of interest. Section 1.3.3 deals with phase sensitive interferometric SNOM measurement. This system is a powerful extension to the regular intensity measurement made with SNOM probes. In section 1.3.4 the applications to PhC structures will be presented with particular emphasis on a point defect microcavity.

1.3.1 The evanescent field on a prism

To begin our discussion of SNOM experiments we will consider the measurement of the evanescent field at the surface of a prism. This is a useful illustration of the ability of SNOM in a simple system. As shown in figure 1.4a, a laser beam illuminates a prism at a super-critical angle and a sharp uncoated optical fibre tip is inserted in the evanescent field at the prism surface to spy on the optical intensity. The tip used in this experiment was an uncoated glass fibre, and the optical detection is performed at the output of the fibre. In terms of the previously defined SNOM modes, this example shows apertureless collection mode SNOM using total internal reflection for illumination.

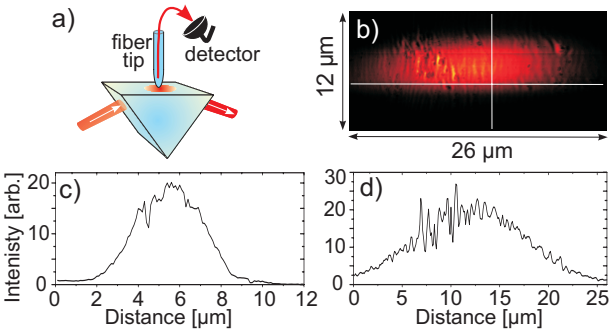

Figure 1.4: a) Experimental arrangement for the detection of evanescent waves on the surface of a prism using SNOM in the collection mode. b) The SNOM image of the laser beam focus. c) A cross section along the vertical axis. d) A cross section along the hoizontal axis.

Figure 1.4b displays the image obtained from the prism surface, whereas figures 1.4c and d show two cross sections from it. The rapid modulations in parts of these figures reveal the high spatial resolution in this image and give direct evidence of subwavelength roughness on the prism surface. This provides a simple first example in our discussion where SNOM offers information that far-field imaging could not have acquired.

1.3.2 SNOM on whispering-gallery resonators

A challenging goal in quantum optical experiments of the past two decades has been to achieve a strong coupling between a single emitter and a high-Q mode of a resonator [44, 45]. Conventional resonators can offer very high quality factors with large mode volumes while the microscopic systems provide very low mode volume with a moderate Q. Ideally, one seeks a system with both low volume and high Q. In our laboratory we have investigated two microresonator systems that have the potential to achieve this goal, namely silica microspheres and photonic crystal point defects. In this section we discuss the properties of silica microspheres and how SNOM can be used to characterize them.

Whispering-gallery modes (WGMs) belong to the larger class of Mie modes in dielectric objects of circular cross section [46]. The characteristic property of a WGM is that light undergoes a large number of total internal reflections before it closes on itself in phase. The losses at each total reflection are negligible compared to those from metallic or even Bragg mirrors. As a result WGMs in silica can reach very high quality factors, up to 10^{10}, limited by absorption [47]. In the 1990s silica microspheres were studied by several groups [48–50]. As shown in figure 1.5a, in order to couple to these modes in an efficient manner, one can use prism coupling and frustrated total internal reflection. As the frequency of the laser is

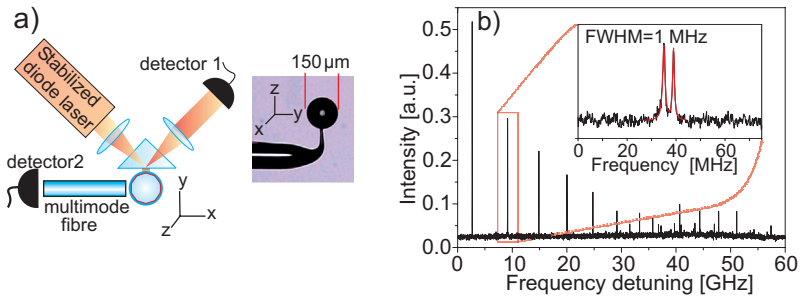

Figure 1.5: a) Top view of the setup for performing spectroscopy on WGMs of a microsphere. An optical microscope image shows a microsphere melted at the end of a pure silica fibre. b) A typical spectrum of WGMs recorded by detector 2 over a frequency range of 60 GHz.

scanned, dips in the transmitted light or peaks in the light scattered from the sphere can be used to detect the resonances.

Three characteristic numbers n, l and m and two polarizations specify in a unique manner each WGM associated with a resonance frequency and spatial mode. The spatial mode is governed by spherical Bessel functions and Legendre polynomials. In general, a given mode could have a large number of nodes and antinodes in the $\vec{r}$ and $\vec{\theta}$ directions. The simplest WGMs circulate in the equatorial plane of the sphere and have one intensity maximum in these directions. The parameter m is degenerate for a perfect sphere. The degeneracy is lifted by the introduction of ellipticity. For a typical microsphere of diameter $100\ \mu m$ fabricated in the laboratory, the resonance frequencies of the modes with identical n and l but different m are spaced by a few GHz. Figure 1.5b shows a spectrum obtained by scanning a narrow-band diode laser and recording the tiny amount of the light that is scattered out of the sphere when a resonance is met. The inset in this figure displays a zoom into one of the resonances, showing two lines as narrow as 1 MHz, implying a quality factor of about 10^8 . The doublet structure is due to the coupling between clockwise and counter clockwise propagating modes [51].

Given the rich and complex composition of the WGM spectrum, identifying a mode based on the frequency information alone would require scanning the laser frequency at least one free spectral range (about 600 GHz) with a high resolution. Alternatively, because the WGMs rely on total internal reflection, an evanescent field exists on the surface of the sphere, and SNOM can be used to interrogate the spatial features of a given WGM along $\vec{\theta}$ and $\vec{\phi}$ [18, 19, 52]. Figure 1.6a shows the schematics of the setup. The sphere-prism distance is set at a few tens to a few hundreds of nanometers. The laser frequency is scanned through the sphere

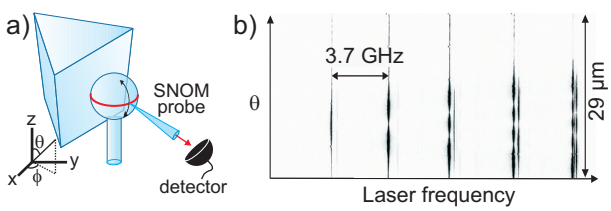

Figure 1.6: a) Schematic view of near-field imaging of WGMs using a tip. b) A spatio-spectral map of WGMs. The fundamental mode with only one intensity maximum in the $\vec{\theta}$ direction is clearly identified. From [52].

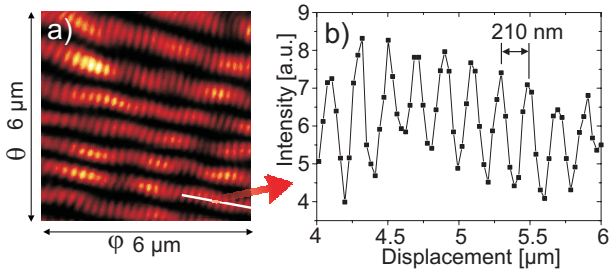

Figure 1.7: A two-dimensional spatial map of a WGM with $l-|m| \gg 1$. The tilt of the microsphere in the xz plane is put in evidence. b) A cross section from a) shows the periodic modulations of the intensity along $\vec{\phi}$.

resonance, and the tip is approached to the sphere surface using the shear-force signal. Figure 1.6b plots a spatio-spectral map of several WGM modes with increasing number of maxima along $\vec{\theta}$. In particular, the fundamental WGM corresponding to $l = m$ is clearly identified. These modes are of special interest because they offer the lowest mode volume, leading to largest effects in quantum optical studies.

By recording the 2D intensity modulations of the WGMs, SNOM can discover subwavelength deviations from their predicted behavior. Figure 1.7a shows a two-dimensional spatial map of a given WGM with $l-|m| \gg 1$. In addition to the expected nodes and antinodes in the $\vec{\theta}$ direction, one finds subwavelength intensity modulations along the perimeter of the sphere (figure 1.7b) [53]. These fast modulations indicate the existence of residual counter propagating waves that lead to standing waves. The periodicity of this pattern allows one to determine the parameter $|m|$ so that together with our knowledge of $l-|m|$ one can also identify l [19].

The combination of high resolution microscopy and spectroscopy allows detailed mapping and characterizing of the mode patterns and frequencies in silica microspheres. Experiments with microspheres are mechanically complex. This work shows that even under such conditions SNOM is a practical addition to the experimental setup. This work also demonstrates that SNOM can make measurements of optically sensitive high-Q devices, although as will be discussed in section 1.4, caution is still required in some circumstances.

1.3.3 Interferometric SNOM measurements

The great majority of SNOM experiments detect field intensities. It has, however, been shown by several groups that by interfering the SNOM signal with a reference laser beam one can obtain valuable information about the field amplitude and phase [21, 54–56]. Here we briefly discuss this technique through two examples of recent work at the University of Twente.

A schematic of the experiment is shown in figure 1.8. Light collected by the SNOM

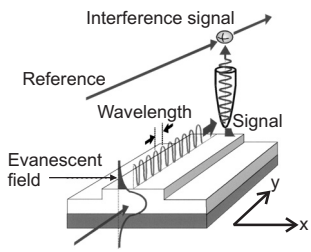

Figure 1.8: Schematic illustration of a heterodyne SNOM setup. The light collected by the SNOM tip is mixed with a frequency shifted reference beam. From [21].

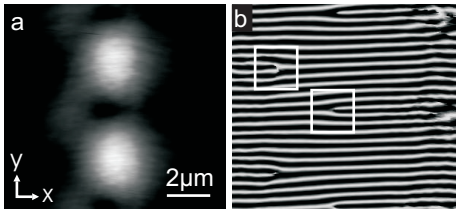

Figure 1.9: a) amplitude of the light inside the waveguide; b) cosine of optical phase of the light inside the waveguide. From [21].

tip is mixed with a frequency shifted reference beam that has been generated using acousto-optic modulation. The resulting signal is detected using a lock-in amplifier. The X and Y quadratures of the lock-in signal then provide the cosine and sine of the phase difference between the SNOM light and the reference beam. As with all interferometric devices, care is required to eliminate signal drift due to thermal and acoustic changes in the interferometer arm lengths, lest the phase signal be swamped by spurious noise.

Figure 1.9 shows the results obtained by Balistreri *et al.* on a waveguide that supports modes with TE and TM polarizations [21]. Figure 1.9a shows the amplitude of the field in a lateral scan (see axes in figure 1.8 for reference.). Figure 1.9b shows the cosine of the phase for the same area. The amplitude of the field inside the waveguide is strongly modulated. There are two distinct lobes along the y direction due to the interference of various TM and TE modes excited in the waveguide. Ideally these should not interfere since they are orthogonal. The detection via the SNOM tip and coupling of polarization modes in the fibre leads, however, to substantial interference. The overall optical phase, shown in figure 1.9b, is seen to correspond to that of a plane wave. There are some points in the phase map, such as those highlighted in the white squares, where the phase fronts appear to meet at a point to form a phase singularity. Taking into account the TE_{00}, TE_{01} and TM_{00} modes, Balistreri *et al.* were able to reconstruct the observed amplitude and phase.

Using the setup depicted in figure 1.8 the propagation of femtosecond pulses in a waveguide has also become accessible to SNOM measurement [22, 23]. Once again acousto-optic modulation has been used to generate the reference beam that is mixed with the signal from the SNOM tip. The important differences are that the cw beams have been replaced with a pulsed laser source and the path length of the reference beam can be accurately tuned. The interference of the reference beam and the SNOM signal will now only occur when their photons arrive at the detector simultaneously. Tuning the path length of the reference beam therefore allows one to choose what part of the waveguide will be imaged. The results are shown in figure 1.10. As the path length of the reference beam is varied in 1.10a-e, the pulse is seen to move from left to right. This measurement allowed direct determination of the group and phase velocities in the waveguide.

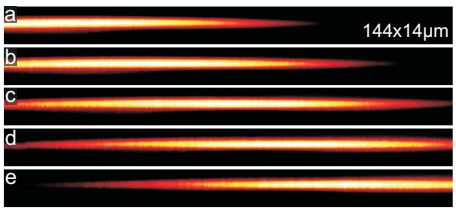

Figure 1.10: The optical field amplitude as measured by the instrument for different positions of the optical delay line. From (a) through (e), the optical path length of the reference branch is increased by $40.0 \pm 0.6\mu$m. This results in steps of the reference time of 133±2fs. From [22].

1.3.4 Photonic crystals

The optical properties of PhCs stem from collective interference between fields scattered by many, many subwavelength dielectric features of the structure. Probing a PhC by transmission and reflection measurements provides valuable information about the propagation of the light through the crystal, however such measurements remain only indirect signatures of how light interacts with the complex geometry of a photonic crystal. To get a visual picture of light propagation in coordinate space numerical simulations such as finite-difference time-domain (FDTD) can be performed, but to really 'see' what happens when light goes through a defect or around a sharp bend in a waveguide we require an imaging scheme. One might imagine using a microscope based on some lenses and a camera [57], but this is not satisfactory for two reasons. First, if the quality of the PhC structure is high, only very little light leaks out into the microscope. More importantly, however, we know from Abbés limit (defined in section 1.2.2) that a far-field microscope cannot resolve features separated by distances below $\lambda/(2n\sin\theta) = \lambda/(2\,NA)$, where $NA = n\sin\theta$ denotes the numerical aperture of the imaging instrument [58]. Near-field microscopy is, therefore, a particularly attractive and valuable tool for studying PhCs. Indeed, this has been recognized by several groups in the past few years. Limited access to high quality PhC fabrication and to sophisticated three-dimensional numerical simulations has, however, seriously hampered the application of SNOM to ultra-high resolution imaging of light confinement in complex PhC structures. In particular, measurements that allow quantitative characterization of PhCs and a robust comparison with theory are just beginning to appear.

One of the early attempts to perform optical near-field measurements on photonic crystal structures was done in the illumination mode and is due to McDaniel *et al.* [29, 30]. As depicted in figure 1.11, in this configuration the evanescent near field of the probe is scattered by the subwavelength features of the PhC surface into many of its modes. As the probe is positioned laterally, the strength of this coupling is varied and the overall transmission is modulated, yielding interesting information about the PhC. In the work done by McDaniel *et al.* the PhC consisted of a deep glass sample with a two-dimensional lattice of pores without a strong photonic band gap effect. Light was sent through a coated tip along the pores and was detected with a large area detector at the other side of the sample. The researchers examined the transmission of the sample as a function of the probe position and wavelength. The illumination mode was also used very recently by Flück *et al.* to investigate a three-dimensional artificial opal photonic crystal [31].

Other earlier reports in the literature include collection mode SNOM on grating-type waveguide structures [32], two-dimensional PhC slabs [33] and deep channel glass struc-

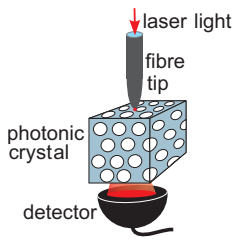

Figure 1.11: Illumination mode SNOM. Light from the fibre is incident on the sample and then detected behind the sample.

tures [34]. In particular the results obtained by Phillips *et al.* [33] nicely show how SNOM can be used to investigate scattering and interference phenomena at the subwavelength scale. An important observation made by these authors, and many other groups, is the difficulty of distinguishing the evanescent fields from propagating components caused by scattering processes that take place away from the tip. A prudent and useful experimental check that helps to discriminate the contribution of the evanescent waves at the surface from those of propagating ones is to record the signal with the tip scanned at different heights above the sample surface. Even so, one has to keep in mind that scattering from a periodic structure yields periodic intensity modulations even at larger tip-sample separations, making it difficult to distinguish the far and the near fields [59]. To minimize the effect of stray light, coated tips have often been used. Furthermore, the sample design and fabrication quality also play important roles in minimizing unwanted scattering at the sample surface.

Theoretical treatments of near-field studies on photonic crystals have been even rarer than the experimental works. The reason lies in the fact that numerical solutions of Maxwell equations are very demanding for systems that impose many boundary conditions at the nanometer scale. To reach a good level of accuracy the system has to be discretized into very small elements so that the computation time quickly reaches days. When dealing with shallow slab type PhCs three-dimensional calculations become manageable. Fan *et al.* [60] have considered such a system that even includes the effect of the SNOM tip. They show that high resolution SNOM images of the intensity modulations could not only portray the path that light takes in the crystal, but also determine frequency/wave-vector dispersion information of the PhC. In order to do this, they suggest exciting modes at different frequencies and propagation directions, and analyzing the resulting modulation patterns.

Some of the most exciting applications of PhCs are based on the introduction of functionalities through the incorporation of defects in the otherwise periodic lattice. Defects influence the photonic band structure of the PhC and can result in the flow or confinement of light along particular pathways in the crystal. A point defect yields a region surrounded by high reflecting mirrors, thereby establishing a microresonator. A line defect could act as waveguide, while combinations of these building blocks could achieve complex units such as interferometers, filters, etc. As was the case for the silica microspheres (see section 1.3.2), the spectral information from PhCs alone cannot determine the spatial extent of the light in them. Here too, SNOM proves to be a very valuable tool.

The first near-field imaging experiment on photonic crystals containing defects was reported by Smith *et al.* in 1993 [35]. The sample was an array of dielectric rods placed in a microwave waveguide structure with one rod missing. A local microwave probe was positioned at different locations at the top of the structure to map the intensity distribution about the point defect. The small length scales required for PhCs in the optical domain make similar experiments more challenging. Aside from the difficulties in the fabrication of high quality PhCs, researchers are also confronted by other technical barriers in the process of characterization. Firstly, the appropriate light source is not always available. In order to couple the light into subwavelength defects, a focusable source like a laser is desirable. Commercially available lasers often lack the required degree of wavelength tunability or have linewidths that are too broad. Secondly, handling and alignment of tiny samples consisting of subwavelength features is not trivial and calls for many motional degrees of freedom in the setup.

A landmark in the unique properties of PhC devices has been the efficient transmission

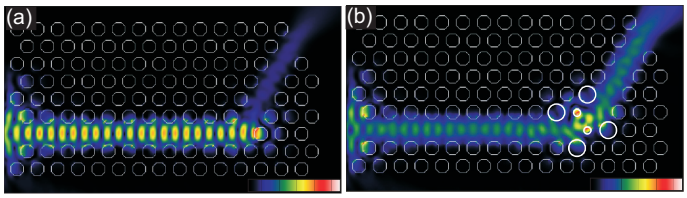

Figure 1.12: 2D FDTD models showing field amplitude. a) A sixty degree bend in a waveguide with poor transmission. b) Modified bend with 96% transmission over a broad frequency range. Parameters: r/a=0.34, $n = 3.43$, $a = 500$ nm, $a/\lambda = 0.2844$. The larger holes in (b) have r/a=0.41 and the smaller holes have r/a=0.17. Polarization mode is TE

of light around sharp bends. Early simulations and experiments showed that transmission at as high as 98% could be achieved around $90°$ bends in PhCs with quadratic lattice [61, 62]. But similar results on PhCs with other designs proved to be less trivial to accomplish, especially if broadband transmission is required [63–65]. Figure 1.12a shows the results of two-dimensional FDTD simulations for the intensity distribution along a waveguide with a $60°$ bend. Most of the light is reflected from the bend, giving rise to standing waves in the incident arm. Figure 1.12b shows that more than 96% of light, at the identical frequency, can be guided around the bend if the diameters of a few holes are modified.

Given the intricacies of the fabrication process and the sensitivity of the PhC performance to fine geometric details, SNOM is almost indispensable for characterization and testing of such devices. Figure 1.13a shows the topography image of a test sample based on InP technology in the preliminary phase of the fabrication [66]. The lattice constant was chosen to be 500nm and the holes had a diameter of 300nm, but their depth profile was not optimized and no capping layer was integrated. As a result the sample is not expected to possess a photonic band gap. Figure 1.13b shows a SNOM image taken with an uncoated fibre tip in collection mode while the beam from a diode laser at $\lambda = 1550nm$ was coupled into the waveguide using a lens with a $N.A. = 0.68$. The image reveals that there exists some guiding in the input waveguide which is expected to be due to index guiding. Moreover, the near-field image nicely puts into evidence that most of the light is reflected at the bend, resulting in the standing waves observed in the entrance arm of the structure. This study gives a good example of the advantage of SNOM in characterizing photonic devices even when numerical results are not available to guide one's intuition.

Bozhevolnyi *et al.* have reported on SNOM investigations of PhC waveguides containing $90°$ bends [36, 37]. Light from a tunable laser at $\lambda = 1500nm$ was coupled into PhC waveguides externally and a coated fibre tip was used to image the propagation of light at

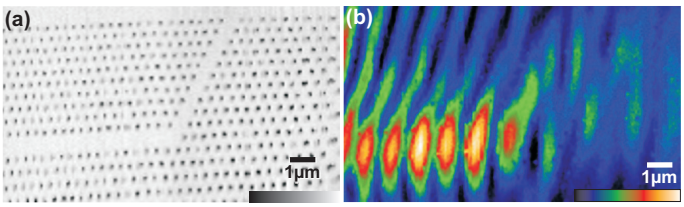

Figure 1.13: a) Topography image of waveguide b) Optical image of the waveguide. Polarization mode is TM.

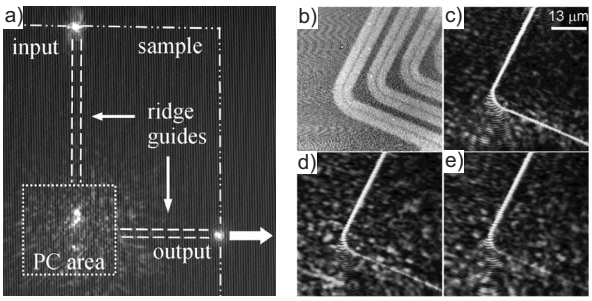

Figure 1.14: a) Far-field image of light scattered from the sample. b) Topographical image taken with SNOM tip. c) Near-field image at λ=1520nm; d) near-field image at λ=1550nm and e) near-field image at λ=1570nm. Weak optical signals have been artificially enhanced in order to improve the visibility of concentric fringes. From [37].

the top surface. Figure 1.14a shows the far-field image of the sample. Three major scattering locations are identified to be at the end junctions of the waveguides and around the bend of the PhC waveguide. Figure 1.14b displays the topography image from parts of three PhC waveguides investigated by SNOM. The images in figures c, d and e show propagation at three different wavelengths of $\lambda = 1520, 1550$ and $1570nm$, respectively. The increase in losses for longer wavelengths is evident. The concentric rings observed in the SNOM images give more insight into the scattering process at the bend. The authors attribute these to the interference between the contributions from the waveguide mode and a quasi-homogeneous coherent background. Figure 1.15a shows a topography zoom of the region around the bend for one waveguide whereas figures 1.15b-f display corresponding SNOM images recorded at different heights above the sample. These images clearly demonstrate that the resolution deteriorates as the tip is removed. The image in figure 1.15b also shows standing waves that have resulted from back reflections in the system.

Another important question that Bozhevolnyi *et al.* addressed was that of the quantitative measurement of the transmission around the waveguide bend. Measurements of absolute transmission through PhC structures are nontrivial because it is difficult to correctly take into account the losses related to the in-coupling process. A working solution has been to use internal light sources and to compare the power out of the waveguide with that out of the unstructured part of the sample [67]. It has also proved possible to use internal cavities formed by residual reflections to measure the loss of a single device [68]. Although such solutions are valuable, they do not provide practical answers to the characterization of a sophisticated device after fabrication. In particular, they do not provide any information about the point-

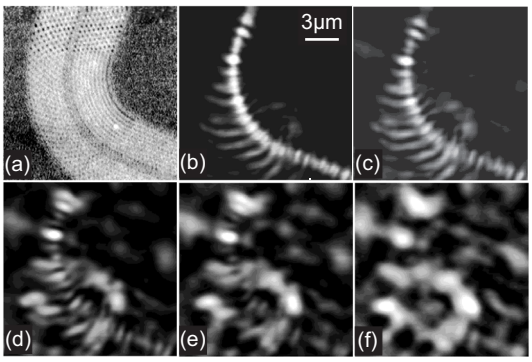

Figure 1.15: a) Topographical image taken with SNOM tip. Images b) to f) show SNOM images at λ=1520nm with different tip-surface separation: b) 10nm (with shear force control); c) 100nm; d) 300nm; e) 500nm and f) 700nm. From [37].

to-point loss, only the sum total. By comparing the SNOM signal before and after a given location, one can directly obtain a quantitative estimate of transmission efficiency through any part of the system.

The last example we treat is that of microresonator studies in our own laboratory. The simplest seeming but also most interesting and challenging configuration of defects in PhCs is the so-called point defect where a single site, for example a pore, is missing. The fundamentally small nature of this microresonator is of great interest for quantum optical effects because a photon confined to such tiny region carries very large electric fields. Needless to say, applications in integrated optics and analytics also welcome very small building blocks. The challenge in the design and realization of PhC microresonators is to maintain the lowest volume and achieve the highest quality factor Q possible. Quality factors as high as a few thousand for point-defect microcavities [69] and 13,000 for a two-point defect in a graded lattice [70] have so far been demonstrated.

Figure 1.16a shows a scanning electron microscope image of a two-dimensional microresonator made of silicon. The structure has a lattice constant of $a = 1.5\mu m$ with a depth of $100\mu m$ and was fabricated by electrochemical preparation of macroporous silicon [71–73]. A point defect is surrounded by two pores and two waveguides that help couple light in and out of the cavity. FDTD calculations predict two sharp resonances at nominal wavelengths of $3.732\mu m$ and $3.957\mu m$ within the fundamental band gap between $3.4\mu m$ and $5.8\mu m$.

We could put these resonances into evidence by coupling in laser light from a continuous-wave optical parametric oscillator and by using a SNOM probe to detect the transmission through [38] and propagation along [39] the structure. Figure 1.16 shows the experimental setup. The laser beam is focused onto the entrance facet of the first waveguide. The sample's position and tilt can be adjusted to optimize the coupling. Some of the light scatters around the sample, leading to unwanted background at the output facet. This prompted us to scan the uncoated fibre tip #1 in a head-on configuration to image the output facet. Figure 1.17a shows an example of the image recorded by this tip. The signal detected cannot be attributed only to evanescent fields. Nevertheless, it is intriguing that the full width at half-maximum (FWHM) of the spot α at the exit facet is about 4 μm, corresponding to only a bit more than λ. The great advantage of this detection scheme can be appreciated when considering the bright spot β which is due to the stray scattered light travelling above the sample. Without a local detector it would have been extremely difficult to discriminate against this signal. By repeating measurements such as 1.17a at different laser frequencies, the experimental resonance wavelengths could be determined to be 3621nm and 3843nm, as shown in figure 1.17b.

Figures 1.18a and b display the intensity distribution expected for the two modes as calculated by two-dimensional FDTD simulations. The very rapid and strong intensity modulations

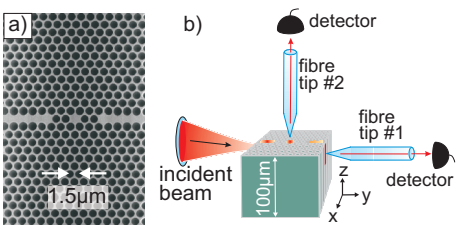

Figure 1.16: a) Top view of a photonic crystal microcavity in macroporous silicon. b)Schematic of the microcavity SNOM setup. Tip 1 is used to detect the output of the cavity while tip 2 is used to scan the surface of the crystal.

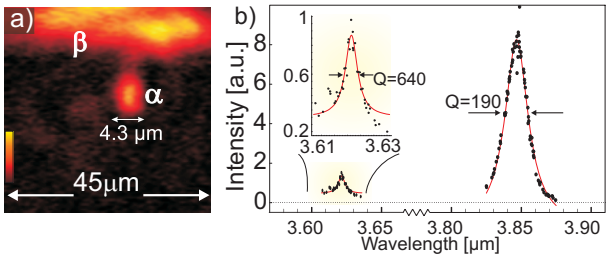

Figure 1.17: a) The light emitted form the photonic crystal as measured using SNOM tip 1. b) The transmission spectrum of the point defect cavity measured using the SNOM tip 1. (b) taken from [38].

at length scales well below a wavelength are the features that one would like to capture with SNOM, but one has to keep in mind that a finite resolution would inevitably cause washing out some details. Figures 1.18c and d show image b after a convolution process with Gaussian filter functions of FWHM 500nm and 1400nm corresponding to $\lambda/7$ and $\lambda/3$ respectively. We remark that, strictly speaking, the choice of this filter is not rigorous. The problem is that the interaction mechanism of a SNOM tip with the sample is neither theoretically nor experimentally known in a quantitative manner. We therefore simply convolve the intensity with a Gaussian filter function. Clearly, any coherent effects or complex polarization dependent processes are neglected in this coarse treatment. Nevertheless, this procedure is very helpful in acquiring intuitive and qualitative understanding of the problem at hand. A comparison of images c and d emphasizes the important role of resolution in optical microscopy.

In order to monitor the propagation of light through the structure and to identify the resonator modes spatially, we use the second SNOM device to probe the crystal's upper surface (see figure 1.16) [39]. Figure 1.19b displays the topography signal of the part of the sample that is examined. This image was recorded using an AFM tip that we mounted at the end of an optical fibre (see probe #2 in figure 1.19a). Another topography image taken by an etched fibre tip is shown in figure 1.19c. The tips used in these experiments were made of fragile fluoride glass and were prone to breakage. For this reason, the probe in this run was not very sharp, leading to a very low lateral topography resolution. We point out that although it is necessary to use very sharp tips for SNOM studies in the visible range, a less pointed fibre tip could still serve as a subwavelength probe for the middle infrared regime. In any event, although the individual pores are not easy to recognize in figure 1.19c, the topography image suffices to identify the two waveguides and the point defect so that one can correlate the optical signal with the PhC structure. Figure 1.19d shows the raw data of the optical intensity signal recorded by near-field probe #2 while the laser wavelength was tuned to the resonance

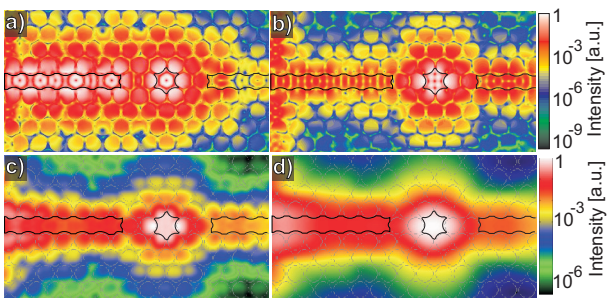

Figure 1.18: a) FDTD model of the intensity of the short wavelength mode in figure 1.17b. b) FDTD model of the intensity of the long wavelength mode in figure 1.17b. c) Convolution of the model in b) with a 500nm detection window. d) Convolution of the model in b) with a 1400nm detection window. a) and b) taken from [38].

at $\lambda = 3.84\mu m$. This data was taken simultaneously to the topography signal of figure 1.19c which we have used together with our knowledge of the scan range to overlap the PhC geometry as a guide to the eye. The propagation of light in the first waveguide and its confinement about the point defect are clearly seen.

The SNOM image in figure 1.19d reveals several properties that are not predicted by the FDTD simulations of figure 1.18b, c or d, i.e. regardless of any resolution considerations. Firstly, the microresonator mode is tilted whereas the image in 1.18b suggests symmetry along the x and y axes. Secondly, the light is pushed to one side by a fraction of a wavelength in the last part of the input waveguide. Thirdly, the measurements reveal subwavelength details of the intensity modulations along this waveguide which again seem to be different from that of figure 1.18. It turns out that these observations indicate small deviations of the PhC structure from its nominal geometry. In fact, electron microscopy studies of macroporous silicon PhCs have shown that one might typically obtain up to 10% fluctuations in the diameters of the pores neighboring the missing pores [74].

Although, as we will see shortly, a quantitative description of the light propagation in a deep PhC requires three-dimensional FDTD calculations, we first consider two-dimensional FDTD simulations for a qualitative understanding of the central phenomena. Figures 1.20a, c and e show three examples of the microresonator mode from figure 1.18b when slight changes are made to the pores surrounding the point defect. The percentage change in pore diameter is indicated in the figures. Figures 1.20b, d and f display the intensity distribution after the consideration of a finite SNOM resolution. In the same manner, the properties of light in the waveguide can also be affected by deviations of pore diameters surrounding the waveguide. Figure 1.20g–l show three examples of light propagation in structures with only two pores being 10% smaller than other holes along the waveguide. The substantial tilt angles of the resonator mode and the sensitive response of the intensity distribution inside the waveguide due to very small modifications of the geometry are impressive. Considering that none of the existing fabrication methods are capable of achieving 100% uniformity of pore geometry, these numerical studies show that the details of light propagation may vary from device-to-device in a substantial manner. SNOM measurements could reveal the subtle differences.

Another interesting aspect of the SNOM image in figure 1.19d is that the light intensity drops dramatically at the surface of the second waveguide. To recover this behavior we performed three-dimensional FDTD calculations. Figure 1.21a shows the intensity distribution at the PhC-air interface for a structure where two holes surrounding the microcavity and two holes along the input waveguide are taken to be 10% smaller than the nominal value. The in-

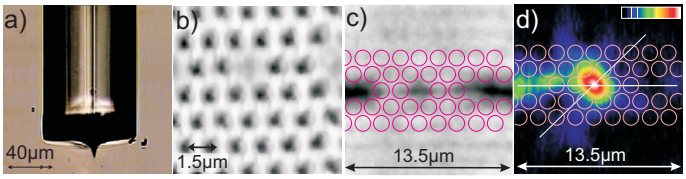

Figure 1.19: a) A SNOM probe with silicon AFM tip mounted on the end. b) Topography signal from combined SNOM/AFM tip showing micro-cavity. c)Topography image taken using etched SNOM tip. d) SNOM image taken simultaneous with c). c) and d) taken from [39].

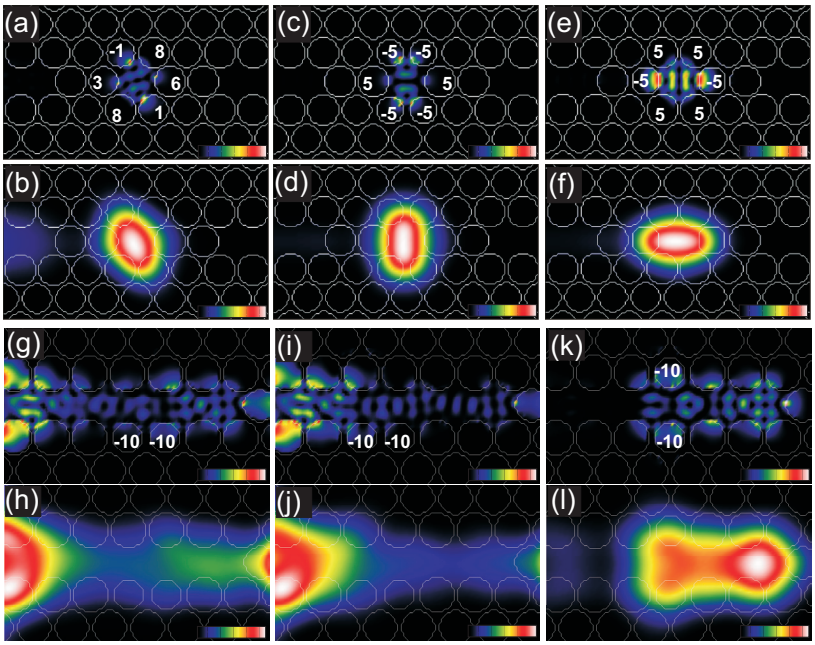

Figure 1.20: (a)–(f): Top pictures show 2D FDTD model of field intensity and the percentage change in the hole size near the cavity. Bottom pictures show the simulated measurement with a tip aperture of 1.4μm. (g)–(l): Top pictures show 2D FDTD model of field intensity and the percentage change in the hole size near the waveguide. Bottom pictures show the simulated measurement with a tip aperture of 1.4μm. Parameters used in this model are r/a=0.437, n=3.43 and a=1.5μm. Dimensionless frequencies are (a,b) 0.3939, (c,d) 0.3746, (e,f) 0.3765, (g,h) 0.3886, (i,j) 0.3886, and (k,l) 0.3931

depth intensity distribution in the yz-plane along the middle of the waveguides and the point defect is displayed in figure 1.21b. After interacting with the point defect the light is pushed downward in the second waveguide so that there is much less light at the surface of the PhC, in agreement with our experimental observation.

Figure 1.21c plots the intensity distribution on the upper surface after convolution with a Gaussian profile of FWHM $1.4\mu m$ corresponding to about $\lambda/3$. The outcome has a striking resemblance with figure 1.19d. The mode is clearly tilted, there are intensity modulations in the waveguide and there is no significant amount of light in the second waveguide. The very good quantitative agreement between the two becomes clear in figures 1.21d and 1.21e where we plot two cross-sections corresponding to those shown in figures 1.21c and 1.19d. Nevertheless, not all aspects of the experimental observations could be recovered. For example, the deflection of light to one side by a few hundred nanometers is not reproduced, the tilt angle of the mode is not identical to the SNOM image, and a very small intensity asymmetry within the microcavity spot remains unexplained. The lack of a full quantitative match between experiment and theory lies in the practical difficulties of three-dimensional calculations that are very time consuming for deep samples.

The PbSe detectors used in this work are not very sensitive. The measurement noise is,

however, so low that a signal-to-noise ratio greater than 100 is obtained. Furthermore, background scattering is insignificant in our experiments. The cross-sections shown in figures 1.21c and d allow us to put a lower limit of 20 to the signal-to-background ratio. This low background is a convincing indication that the field on the upper surface of the PC is evanescent and that although our deep photonic crystal does not confine light in the third dimension, we do not detect propagating fields along the z-axis at the PC-air interface. To this end, we believe that even at a moderate resolution of $\lambda/3$ the SNOM image of figure 1.19d provides features that could reveal small variations of the PhC structure from its nominal parameters.

Other recent experiments have also studied PhC microcavities with SNOM in the collection mode. Gerard *et al.* [40] examined a hexagonal ring cavity of fairly large area using uncoated fibre tips, Shin *et al.* [41] probed a large area PhC laser also with uncoated tips, while Okamoto *et al.* [42] have imaged the light distribution around a point defect using apertured tips. These experiments took advantage of the near infrared luminescence of internal light sources such as quantum wells. The active region is pumped optically and the luminescence light is sent to a detector via the SNOM tip and spectral filters. Okamoto *et al.* could examine the polarization dependence of nondegenerate modes of their microcavity and also used the SNOM tip for the near-field excitation of the luminescence. When working with internal light sources it has to be borne in mind that although the high index of refraction of semiconductor material keeps most of the luminescence within the structure, a considerable amount of light can escape perpendicular to the PhC face. This introduces a certain level of propagating background light that adds to the signal obtained from evanescent fields, deteriorating the signal-to-noise ratio in this configuration. This issue is of much less concern when the active medium undergoes lasing action. Indeed Shin *et al.* have performed extensive far-field and near-field studies of the laser modes in a large area PhC microcavity. These authors used uncoated fibre tips in order to minimize the influence of the tip (see section 1.4) and investigated the intensity distribution in different modes at different emission wavelengths.

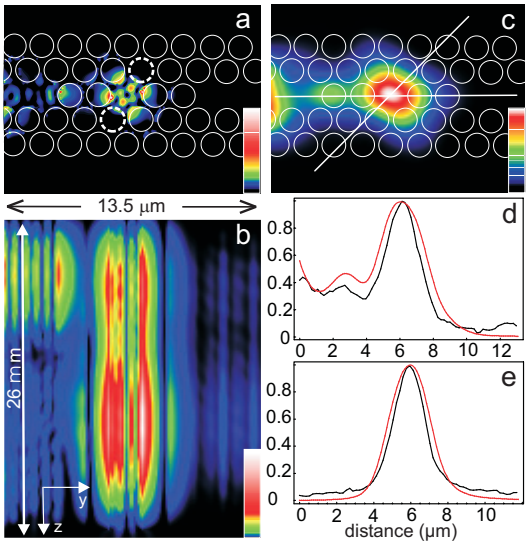

Figure 1.21: a) 3D FDTD model of the field intensity at the crystal surface with indicated holes 10% smaller than nominal value and the waveguide configured as shown in figure 1.20i. b) 3D FDTD model of the field intensity as a function of depth through the crystal. Cross section is taken along the centre of the structure. c) Modelled intensity after convolution with 1.4μm detection window. Images d) and e) show a comparison of theoretical and experimental cross-sections along the waveguide and diagonal to the waveguide respectively. Black is experimental data, red is theoretical. From [39].

1.4 Manipulating Photonic Devices with SNOM

The last issue that we address has to do with the question of whether the tip perturbs the device operation. The short answer is that it certainly could, but mostly it does not. The volume of the SNOM probe inserted in the evanescent field is of the order of $(100\mathrm{nm})^3$. If the scattering caused by this nano-object is comparable or larger than the other types of loss in the system, we can expect a considerable change in the performance of the device during the measurement. In order to minimize the perturbation, it is helpful to use finer tips which are of course also desirable because of offering higher spatial resolution. This in turn requires a sensitive detection as the signal strength drops rapidly as the tip size is reduced.

A concrete example of device perturbation due to SNOM can be given in the case of silica microspheres. In figure 1.22a we see how a micron-sized tip can degrade the quality factor of a fundamental mode ($l = m$) while figure 1.22b shows how the insertion of a fine tip into the evanescent fields at the sphere surface could do no harm for a Q of 10^8 [52]. In the same spirit a certain tip perturbs a mode with a larger volume less than another mode with the same quality factor but a smaller volume.

In addition to introducing losses, the insertion of a small object changes the local index of refraction and therefore the optical path which could in turn modify the frequency spectrum. Figures 1.22c and d display examples of such an effect when a 1μm tip is positioned at different regions of two high-Q WGM modes with $l = m$ and $l - m = 1$ [52, 75]. The horizontal axis denotes the WGM resonance frequency, the vertical axis shows the scan distance in the $\vec{\theta}$ direction while the gray-scale indicates the intensity detected through the tip. The resonance frequency is clearly shifted when the tip is placed at the antinode.

In the case of photonic crystals there are no concrete experimental studies of the tip influence to this date. For imaging purposes it is certainly advantageous to use fine tips. The tip influence will be especially notable when light is confined to a very small region because then the local light intensity increases and the ratio of the tip scattering rate to other losses becomes more important. This could be the case for single point defect microcavities of very high Q in slab photonic crystals. Measurements on extended structures such as waveguides, on the other hand, shouldn't pose serious problems.

The influence of a dielectric tip could be also used in an advantageous configuration. Here it might be possible to fine-tune the PhC spectra by introducing a tip. Figure 1.23a depicts the

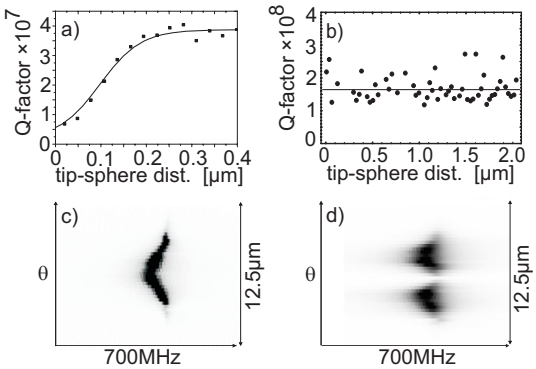

Figure 1.22: a) An uncoated fibre of diameter 2 micrometer affects the quality factor of a fundamental WGM when it is placed within the evanescent range of the sphere surface. b) A fine fibre tip with a radius of curvature of about 100nm leaves the Q unchanged. c-d) The introduction of a 1μm fibre tip in the intensity maxima of WGMs results in tuning their resonance frequencies. From [52].

schematic arrangement of a thought experiment where a silicon tip is used to introduce a local defect. The depth and the size of the tip could then control the extent of the perturbation. The combination of such configurations involving scanning probe techniques such as AFM could offer attractive opto-mechanical devices.

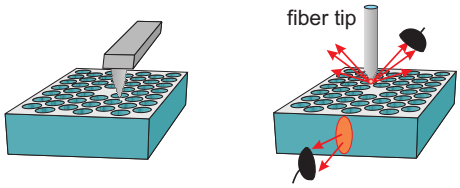

Figure 1.23: a) Arrangement for manipulating the photonic crystal with an AFM tip. b) Arrangement for coupling a nano-emitter mounted at the end of a tip to a photonic crystal microcavity.

1.5 Conclusion

The results presented here show that SNOM has a vital role to play when it comes to characterizing photonic crystal devices. The light inside a photonic crystal is modulated at the subwavelength scale and SNOM is the only technique that can actually image these behaviours. The key advantage of being able to resolve such fine detail is being able to directly compare experimental results with numerical models. Another important feature is the ability to measure from the surface of the crystal, thereby allowing measurement of point-to-point loss. We believe, furthermore, that SNOM is sensitive enough to demonstrate optical effects due to the tiny, but inevitable, imperfections in device fabrication. Direct measurement of these effects will allow refinement and optimization of device design. Finally, experiments carried out so far on silica microspheres and ridge waveguide structures point the way for future applications to photonic crystal structures involving phase sensitive measurements and combinations of spectroscopy and microscopy.

The applications of scanning probe techniques to photonic crystals is still in its infancy. Aside from imaging the flow of light, there are many modes of operation yet to be explored. One such possibility is the direct manipulation of photonic crystal devices using a local probe. This could lead to active control of devices by creating or removing defects on demand (see figure 1.23a). A second path to follow would be the application of SNOM techniques to control the coupling of atoms and light. Figure 1.23b sketches a possible arrangement where the a tip is used to position a nano-emitter [76, 77] with respect to a photonic crystal microcavity, where cavity QED effects may be observable. Similar experiments on silica microspheres have already begun to bear fruit in our laboratories [78].

Acknowledgments

We are grateful to Albert Birner, Ralf Wehrspohn and Ulrich Gösele for collaborating on PhCs made of macroporous silicon. We also thank Robert Wüest, Robert Franck and Daniel Erni at ETH for providing us with InP-based slab PhCs. We acknowledge many fruitful discussions with Mario Agio and Costas M. Soukoulis and thank Wolfgang Stumpf for help with some of the recent measurements. We thank Niek van Hulst and Sergei Bozhevolnyi for kindly providing us with the artwork of their results. Finally we are grateful to the Deutsche Forschungsgemeinschaft (DFG) for the generous support of our research.

References

[1] D. W. Pohl, W. Denk and M. Lanz, *Appl. Phys. Lett.*, 44, 651 (1984).

[2] A. Lewis, M. Isaacson, A. Harootunian and A. Muray, *Ultramicroscopy*, 13, 227 (1984).

[3] R. Toledo-Crow, P. C. Yang, Y. Chen and M. Vaez-Iravani, *Appl. Phys. Lett*, 60, 2957 (1992).

[4] E. Betzig, P. L. Finn and J. S. Weiner, *Appl. Phys. Lett*, 60, 2484 (1992).

[5] E. Betzig and R. J. Chichester, *Science*, 262, 1422 (1993).

[6] M. A. Paesler and M. P. J, *Near-Field Optics: Theory, Instrumentation, and Applications*, Wiley-Interscience (1997).

[7] V. Sandoghdar, *Proc. of the International School of Physics, IOS Press Amsterdam*, pages 65–119 (2001).

[8] J. W. P. Hsu, *Mat. Sci. Eng.*, 33, 1 (2001).

[9] J. J. Greffet and R. Carminati, *Prog. Surf. Sci.*, 56, 133 (1997).

[10] D. W. Pohl, in C. J. R. Sheppard and T. Mulvey, eds., *Advances in Optical and Electron Microscopy*, pages 243–312, Academic Press, London (1991).

[11] E. Abbe, *Archiv. f. Mikroskopische Anat.*, 9, 413 (1873).

[12] K. Iizuka, *Elements of photonics*, volume 1, Wiley-Interscience (2002).

[13] K. Karrai and R. D. Grober, *Appl. Phys. Lett.*, 66, 1842 (1995).

[14] F. Zenhausern, M. P. O'Boyle and H. K. Wickramasinghe, *Appl. Phys. Lett.*, 65, 1623 (1994).

[15] R. C. Reddick, R. J. Warmack and T. L. Ferrell, *Phys. Rev. B*, 39, 767 (1989).

[16] D. Courjon, K. Sarayeddine and M. Spajer, *Opt. Comm.*, 71, 23 (1989).

[17] A. G. Choo, H. E. Jackson, U. Thiel, G. N. D. Brabander and J. T. Boyd, *Appl. Phys. Lett.*, 65, 947 (1994).

[18] J. C. Knight, N. Dubreuil, V. Sandoghdar *et al.*, *Opt. Lett.*, 20, 1515 (1995).

[19] J. C. Knight, N. Dubreuil, V. Sandoghdar *et al.*, *Opt. Lett.*, 21, 698 (1996).

[20] S. Bourzeix, J. M. Moison, F. Mignard *et al.*, *Appl. Phys. Lett.*, 73, 1035 (1998).

[21] M. L. M. Balistreri, J. P. Korterik, L. Kuipers, and N. F. van Hulst, *Phys. Rev. Lett*, 85, 294 (2000).

[22] M. L. M. Balistreri, H. Gersen, J. P. Korterik *et al.*, *Science*, 294, 1080 (2000).

[23] H. Gersen, J. P. Korterik, N. F. van Hulst and L. Kuipers, *Phys. Rev. E*, 68, 026604 (2003).

[24] C. Lienau, A. Richter, A. Klehr and T. Elsaesser, *Appl. Phys. Lett.*, 69, 2471 (1996).

[25] I. Hörsch, R. Kusche, O. Marti, B. Weigl and K. J. Ebeling, *J. Appl. Phys.*, 79, 3831 (1996).
[26] M. L. M. Balistreri, J. W. Klunder, F. C. Blom *et al.*, *Opt. Lett.*, 24, 1829 (1999).
[27] G. H. V. Rhodes, B. B. Goldberg, M. S. Ünlü, S.-T. Chu and B. E. Little, *IEEE J. Selec. Top. Quant. Elect.*, 6, 46 (2000).
[28] J. D. Mills, C. W. J. Hillman, W. S. Brocklesby and B. H. Blott, *Appl. Phys. Lett.*, 75, 4058 (1999).
[29] E. B. McDaniel, J. W. P. Hsu, L. S. Goldner *et al.*, *Phys. Rev. B*, 55, 10878 (1996).
[30] G. W. Bryant, E. L. Shirley, L. S. Goldner *et al.*, *Phys. Rev. B*, 58, 2131 (1998).
[31] E. Flück, N. F. van Hulst, W. L. Vos and L. Kuipers, *Phys. Rev. E*, 68, 15601(R) (2003).
[32] G. H. Vander-Rhodes, M. S. Unlu, B. B. Goldberg, J. M. Pomeroy and T. F. Krauss, *IEE Proc. Optoelectr.*, 194, 379 (1998).
[33] P. L. Phillips, J. C. Knight, B. J. Mangan *et al.*, *J. Appl. Phys.*, 85, 6337 (1999).
[34] A. L. Campillo, J. W. P. Hsu, C. A. Whiteand and A. Rosenberg, *J. Appl. Phys.*, 89, 2801 (2000).
[35] D. R. Smith, R. Dalichaouch, N. Kroll *et al.*, *J. Opt. Soc. Am. B*, 10, 314 (1993).
[36] S. I. Bozhevolnyi, V. S. Volkov, J. Arentoft *et al.*, *Opt. Commun.*, 212, 51 (2002).
[37] S. I. Bozhevolnyi, V. S. Volkov, T. Søndergaard *et al.*, *Phys. Rev. B*, 66, 235204 (2002).
[38] P. Kramper, A. Birner, M. Agio *et al.*, *Phys. Rev. B*, 64, 233102 (2001).
[39] P. Kramper, M. Kafesaki, C. M. Soukoulis *et al.*, *To appear in Opt. Lett.* (2003).
[40] D. Gerard, L. Berguiga, F. de Fornel *et al.*, *Opt. Lett.*, 27, 173 (2002).
[41] Dong-Jae-Shin, Se-Heon-Kim, Jeong-Ki-Hwang *et al.*, *IEEE J. Quantum Elect.*, 38, 857 (2002).
[42] K. Okamoto, M. Lončar, T. Yoshie *et al.*, *Appl. Phys. Lett.*, 82, 1676 (2003).
[43] B. Buchler, P. Kramper, M. Kafesaki, C. M. Soukoulis and V. Sandoghdar, *Submitted to IEICE Trans. Electron.*
[44] H. Kimble, *Physica Scripta*, T76, 127 (1998).
[45] A. Kiraz, C. Reese, B. Gayral *et al.*, *J. Opt. B*, 5, 129 (2003).
[46] C. F. Bohren and D. R. Huffman, *Absorption and Scattering of Light by Small Particles*, John Wiley and Sons (1983).
[47] M. L. Gorodetsky, A. A. Savchenkov and V. S. Ilchenko, *Opt. Lett.*, 21, 453 (1996).
[48] V. B. Braginsky, M. L. Gorodetsky and V. S. Ilchenko, *Phys. Lett. A*, 137, 393 (1989).
[49] L. Collot, V. Lefevre-Seguin, M. Brune, J. Raimond and S. Haroche, *Eur. Phys. Lett.*, 23, 327 (1993).
[50] D. W. Vernooy, A. Furusawa, N. P. Georgiades, V. S. Ilchenko and H. J. Kimble, *Phys. Rev. A*, 57, R2293 (1998).
[51] D. S. Weiss, V. Sandoghdar, J. Hare *et al.*, *Opt. Lett.*, 20, 1835 (1995).
[52] S. Götzinger, O. Benson and V. Sandoghdar, *Appl. Phys. B*, 73, 825 (2001).
[53] S. Götzinger, S. Demmerer, O. Benson and V. Sandoghdar, *J. Microsc.*, 202, 117 (2001).
[54] M. Vaez-Iravani and R. Toledo-Crow, *Appl. Phys. Lett.*, 62, 1044 (1993).
[55] J. Walford, K. Nugent, A. Roberts and R. Scholten, *Appl. Opt*, 38, 3508 (1999).

[56] P. L. Phillips, J. C. Knight, J. M. Pottage, G. Kakarantzas and J. St. P. Russell, *Appl. Phys. Lett.*, 76, 541 (2000).

[57] M. Lončar, D. Nedeljković, T. P. Pearsall *et al.*, *Appl. Phys. Lett.*, 80, 1689 (2002).

[58] M. Born and E. Wolf, *Principles of Optics: Electromagnetic Theory of Propagation, Interference and Diffraction of Light*, 7th edition (1999).

[59] M. Mansuripur, *Classical Optics and its Applications*, Cambridge University Press (2002).

[60] S. Fan, I. Appelbaum and J. D. Joannopoulos, *Appl. Phys. Lett.*, 75, 3461 (1999).

[61] A. Mekis, J. C. Chjen, I. Kurland *et al.*, *Phys. Rev. Lett.*, 77, 3787 (1996).

[62] S.-Y. Lin, E. Chow, V. Hietala, P. R. Villeneuve and J. D. Joannopoulos, *Science*, 282, 274 (1998).

[63] E. Chow, S. Y. Lin, J. R. Wendt, S. G. Johnson and J. D. Joannopoulos, *Opt. Lett.*, 26, 286 (2001).

[64] A. Chutinan, M. Okano and S. Noda, *Appl. Phys. Lett.*, 80, 1698 (2002).

[65] H. Benisty, S. Olivier, C. Weisbuch *et al.*, *IEEE J. Quant. Electon.*, 38, 770 (2002).

[66] R. Wüest, P. Strasser, M. Jungo *et al.*, *Microelectron. Eng.*, 67-68, 182 (2003).

[67] H. Benisty, C. Weisbuch, D. Labilloy *et al.*, *J. Lightwave. Technol.*, 17, 2063 (1999).

[68] A. Talneaua, M. Mulot, S. Anand and P. Lalanne, *Appl. Phys. Lett.*, 82, 2577 (2003).

[69] T. Yoshie, J. Vučković, A. Scherer, H. Chen and D. Deppe, *Appl. Phys. Lett.*, 79, 4289 (2001).

[70] K. Srinivasan, P. E. Barclay, O. Painter *et al.*, *Appl. Phys. Lett.*, 83, 1915 (2003).

[71] V. Lehmann, *J. Electrochem. Soc.*, 140, 2836 (1993).

[72] A. Birner, U. Grüning, S. Ottow *et al.*, *Phys. Stat. Sol. A*, 165, 111 (1998).

[73] J. Schilling, R. B. Wehrspohn, A. Birner *et al.*, *J. Opt. A: Pure Appl. Opt.*, 3, S121 (2001).

[74] A. Birner, Ph.D. thesis, Martin-Luther University at Halle-Wittenberg (2000).

[75] S. Götzinger, O. Benson and V. Sandoghdar, *Opt. Lett.*, 27, 80 (2002).

[76] J. Michaelis, C. Hettich, J. Mlynek and V. Sandoghdar, *Nature*, 405, 325 (2000).

[77] S. Kühn, C. Hettich, C. Schmitt, J.-P. Poizat and V. Sandoghdar, *J. of Microscopy*, 202, 2 (2001).

[78] S. Götzinger, L. de S. Menezes, A. Mazzei *et al.* (Submitted 2003).